

Magnetic Domain-Wall Tilting due to Domain-Wall Speed Asymmetry

Dae-Yun Kim¹, Min-Ho Park¹, Yong-Keun Park^{1,2}, Joo-Sung Kim¹, Yoon-Seok Nam¹, Hyun-Seok Hwang¹, Duck-Ho Kim^{1,3}, Soong-Geun Je^{1,4}, Byoung-Chul Min², and Sug-Bong Choe^{1†}

¹Department of Physics and Institute of Applied Physics, Seoul National University, Seoul, 08826, Republic of Korea.

²Center for Spintronics, Korea Institute of Science and Technology, Seoul, 02792, Republic of Korea.

³Institute for Chemical Research, Kyoto University, Kyoto, 611-0011, Japan.

⁴CNRS, SPINTECH, F-38042 Grenoble, France.

[†]Correspondence to: sugbong@snu.ac.kr

Chiral magnetic materials provide a number of challenging issues such as the highly-efficient domain-wall (DW) and skyrmion motions driven by electric current [1-4], as of the operation principles of emerging spintronic devices [5-7]. The DWs in the chiral materials exhibit asymmetric DW speed variation under application of in-plane magnetic field [8, 9]. Here, we show that such DW speed asymmetry causes the DW tilting during the motion along wire structure. It has been known that the DW tilting can be induced by the direct Zeeman interaction of the DW magnetization under application of in-plane magnetic field [10, 11]. However, our experimental observations manifests that there exists another dominant process with the DW speed asymmetry caused by either the Dzyaloshinskii–Moriya interaction (DMI) [9] or the chirality-dependent DW speed variation [12-17]. A theoretical model based on the DW geometry reveals that the DW tilting is initiated by the DW pinning at wire edges and then, the direction of the DW

tilting is determined by the DW speed asymmetry, as confirmed by a numerical simulation. The present observation reveals the decisive role of the DW pinning with the DW speed asymmetry, which determines the DW geometry and consequently, the dynamics.

The DMI—an antisymmetric exchange interaction [18, 19]—has been actively studied nowadays due to its important role in spintronics such as formation of the magnetic skyrmions [3, 4, 20] or stabilization of the chiral domain-walls (DWs) [8, 21]. To quantify the DMI, several techniques have been developed based on the measurements of asymmetric DW speed [9, 22], the current-induced DW motion [23, 24], asymmetric hysteresis of magnetic patterns [25], and Brillouin light scattering [26]. Fairly recently, a theoretical study proposed another DMI measurement scheme based on the DW tilting in magnetic wire structure under application of in-plane magnetic field [10, 27]. It is obvious that, due to the Zeeman interaction between the in-plane magnetic field and the magnetization inside the DW, the DW has to be tilted to an equilibrium angle of minimum energy configuration. The equilibrium angle is determined by the counterbalance between the DMI and Zeeman energies. The present work was originally motivated to verify this prediction experimentally, but interestingly, we found the existence of another governing mechanism that overwhelms the prediction based on the energy minimization.

Results

Observation of DW tilting

Figure 1(a) plots the DW speed v_{DW} with respect to the in-plane magnetic field H_x for Sample I, where H_{\perp} is applied normal to the DW (for sample details, see methods). The plot

clearly shows that v_{DW} has a minimum at H_0 (blue vertical line) and exhibits a symmetric variation around H_0 . According to Refs. [8, 9], the value of H_0 is a direct measure of the DMI-induced effective magnetic field H_{DMI} , since the minimum v_{DW} appears at the Bloch-type DW configuration under zero total magnetic field i.e. $H_{\text{DMI}} + H_0 = 0$. Therefore, from the present measurement, H_{DMI} is quantified as -120 ± 5 mT in the direction normal to the DW. Due to the large negative H_{DMI} , the magnetization M_{DW} inside the DW is aligned parallel to H_{DMI} , forming the Néel-type DW configuration as depicted in Fig. 1(b). At this instant, if one applies an additional in-plane magnetic field H_y in the direction transverse to the wire, the Zeeman interaction will rotate M_{DW} , followed by tilting of the overall DW to keep the Néel-type DW configuration [10]. For the present sample with a negative H_{DMI} , it is expected that the DW has to rotate clockwise under application of H_y (> 0) as shown by Fig. 1(c).

However, the experimental observation is opposite to the above prediction. Figure 1(d) shows the DW images after each successive application of out-of-plane magnetic field H_z pulses. The first three images were taken without application of H_y and the last three images were taken under application of H_y . The figure clearly shows the DW tilting between these two sorts of images, conforming that the tilting is truly caused by application of H_y (> 0). However, it is surprising to note that the direction of the DW tilting is counterclockwise, which is opposite to the prediction shown by Fig. 1(c). The present experimental observation, therefore, indicates that there should exist another hidden governing factor of the DW tilting.

DMI-induced DW tilting with edge pinning

It is also interesting to note that the DWs with $H_y = 0$ show a typical shape of circular arcs.

Such typical DW shape indicates the existence of pinning at the edges of wire [28, 29]. The subsequent effect from such arc formation can be explained as follows. Figure 2(a) depicts the typical DW shape of a circular arc. Due to the shape of arc, if one applies H_y (blue arrows), the component H_\perp (black arrows) normal to the DW varies on position. Then, due to the v_{DW} dependence on H_\perp as shown by Fig. 1(a), v_{DW} also varies accordingly. For this sample, the upper and lower parts of the DW have positive and negative H_\perp , respectively, as shown by Fig. 2(a). Therefore, the upper part moves slower than the lower part and consequently, the overall DW shape rotates counterclockwise. One can therefore conclude that the pinning effect can trigger the DW tilting, of which the direction accords to the experimental observation.

For better insight, we consider the role of H_{DMI} in the above process. Due to the shape of the arc, the direction of H_{DMI} (red arrows) varies on position to keep the direction normal to the DW. If one applies H_y here, due to the different angles between H_{DMI} and H_y , M_{DW} should rotate differently, resulting in non-uniform distribution of the DW energy density σ_{DW} . According to Ref. [8, 9], σ_{DW} is given as

$$\sigma_{\text{DW}} = \sigma_0 + 2\lambda K_D \cos^2 \psi - \pi\lambda M_S [(H_\perp + H_{\text{DMI}}) \cos \psi + H_\parallel \sin \psi], \quad (1)$$

with the Bloch-type DW energy density σ_0 , the DW width λ , the DW anisotropy energy density K_D , and the saturation magnetization M_S , where H_\parallel is the component of H_y parallel to the DW and ψ is the angle of M_{DW} from the direction normal to the DW. For general case, the equilibrium ψ is determined by the energy minimization condition for a given H_y .

Though there is no explicit analytic solution of Eq. (1) with the equilibrium ψ , one can intuitively estimate σ_{DW} for the case of a large negative H_{DMI} as of Sample I, since $\cos \psi$ is almost set to -1 and does not change much under the experimental range of H_y . For this case, one can readily obtain a simplified relation

$$\sigma_{\text{DW}} \approx \sigma_0 + \pi \lambda M_S (H_{\perp} + H_{\text{DMI}}). \quad (2)$$

Then, according to Ref. [9], v_{DW} depends on σ_{DW} via the DW creep criticality

$$v_{\text{DW}} = v_0 \exp[-\alpha(\sigma_{\text{DW}}/\sigma_0)^{1/4} H_z^{-1/4}], \quad (3)$$

where v_0 is the characteristic speed and α is the scaling constant [30]. These relations can explain the v_{DW} dependence on H_{\perp} : a larger H_{\perp} has a larger σ_{DW} and consequently, a smaller v_{DW} in accordance to Fig. 1(a). One can therefore reach the same conclusion that the upper part of the DW with positive H_{\perp} moves slower than the lower part with negative H_{\perp} and consequently, the overall DW exhibit counterclockwise tilting.

To confirm the present prediction, we carried out a numerical simulation based on Eqs. (1) and (3) by including consideration of the local pinning force f_{pin} . In the simulation, f_{pin} is given as

$$f_{\text{pin}} = \begin{cases} f_{\text{film}} + \beta(y)f_{\text{edge}} & \text{near edges} \\ f_{\text{film}} & \text{otherwise} \end{cases}, \quad (4)$$

where $\beta(y) < 1$, to mimic the edge pinning qualitatively. Since α is proportional to f_{pin} [30-32], one can replace α by $\alpha_0 f_{\text{pin}}$, where α_0 is a constant irrespective of f_{pin} . Then, v_{DW} depends now on f_{pin} . Figure 2(b) shows the simulation results for the case that f_{pin} at the edge is given by 12 % larger than f_{pin} at the center of the wire (for details, see Supplementary I). It is clear from the figure that the counterclockwise DW tilting is well reproduced in accordance to the experimental observations.

It is worthwhile to note that, for the case of a large positive H_{DMI} , $\cos \psi$ is set to +1 and thus, the previous v_{DW} dependence on H_{\perp} becomes reversed, resulting in clockwise DW tilting. Therefore, one can conclude that the DW tilting itself is triggered by the edge DW

pinning, but the direction of the DW tilting is determined by the sign of H_{DMI} .

It is also experimentally confirmed that, for the case that $H_{\text{DMI}} = 0$, the DW tilting does not take place, as expected. Figure 3(a) plots v_{DW} with respect to H_{\perp} for the Sample II (for sample details, see methods). The result shows that H_0 for minimum v_{DW} is almost zero, revealing that $H_{\text{DMI}} \approx 0$ for this sample. Due to the symmetric v_{DW} variation around $H_{\perp} = 0$, the lower and upper parts of the DW moves with the same speed irrespective of the sign of H_{\perp} . Therefore, the DW keeps basically the same shape of the symmetric circular arcs even after application of H_y as seen in Fig. 3(b).

DW tilting by chirality-induced v_{DW} asymmetry

In addition to the DMI-induced v_{DW} variation, many groups have recently uncovered the existence of the chirality-induced v_{DW} variation [12-17]. Here, we explore the effects of such chirality-induced v_{DW} variation on the DW tilting mechanism. For this purpose, the DW tilting is observed from a sample that has nearly zero H_{DMI} , but exhibits sizeable chirality-induced v_{DW} variation.

Figure 4(a) plots the spin-torque efficiency ε_{ST} with respect to H_{\perp} for Sample III (for sample and measurement details, see methods and Supplementary II). Since the plot shows the typical spin-orbit-torque-driven behavior [23], the intercept (red vertical arrow) to the abscissa axis directly quantifies H_{DMI} [23, 33]. The plot thus indicates that H_{DMI} of the present sample is nearly zero ($= 5 \pm 5$ mT), similarly to Sample II. However, very interestingly, in contrast to the invariant DW shape in Sample II, this sample exhibits clear DW tilting as shown by Fig. 4(b), even though both the samples have nearly zero H_{DMI} . Therefore, the DW tilting is not governed by H_{DMI} for the present sample.

To explore the governing factor of the present DW tilting, the v_{DW} variation with respect to H_{\perp} is measured as shown by Fig. 4(c). The results clearly show that the present sample exhibits asymmetric v_{DW} variation, in contrast again to the symmetric variation of Sample II. Such asymmetric v_{DW} variation is possibly caused by the chirality dependent mechanisms such as the chiral damping [13, 14] and asymmetric DW width variation [15] even without the DMI. According to the previous discussion, such asymmetric v_{DW} variation can cause the DW tilting via the difference of v_{DW} between the upper and lower parts of the DW. Therefore, one can deduce that the DW tilting in the present sample is governed by the asymmetric v_{DW} variation, which is possibly caused by the chirality-induced mechanisms [12-17].

Since the slope of the v_{DW} variation near $H_{\perp} = 0$ is opposite to that of Sample I (Fig. 1(a)), the direction of the DW tilting of the present sample should be also opposite to that of Sample I. The present sample thus exhibits clockwise DW tilting, as confirmed by the experimental observation from Fig. 4(b). Therefore, it is general to conclude that the direction of the DW tilting is determined directly by the v_{DW} asymmetry, whatever the origin of the asymmetry—either the DMI [9] or chirality-induced mechanisms [12-17]—is.

DW tilting by both DMI and chirality-induced v_{DW} asymmetry

Finally, as a general case, we examine the case that the sample has both a sizable DMI and chirality-induced v_{DW} variation. Figure 5(a) plots ε_{ST} with respect to H_x for Sample IV (for sample details, see methods). The typical spin-orbit-torque-driven behavior again quantifies H_{DMI} [23] as about -110 ± 5 mT. This sample exhibits also the chirality-induced asymmetric v_{DW} variation with respect to H_{\perp} as shown by Fig. 5(b).

It is intriguing to see that the direction of the DW tilting is reversed depending on the magnitude of applied H_y . Figure 5(c) shows the observation results. The first two images were captured under application of a smaller H_y ($= 50$ mT), whereas the last two images were captured under application of a larger H_y ($= 200$ mT). It is clearly seen from the figure that the directions of the DW tilting are opposite between these two cases: counterclockwise DW tilting for the smaller H_y in contrast to the clockwise DW tilting for the larger H_y . Figure 5(d) summarizes the DW tilting angle θ_{tilt} with respect to H_y . The plot shows that θ_{tilt} is reversed across a threshold magnetic field H_y^{th} (green vertical line). Therefore, a counterclockwise DW tilting appears when $H_y < H_y^{\text{th}}$, otherwise a clockwise DW tilting appears.

The present peculiar results can be explained by considering the asymmetric v_{DW} variation with respect to H_{\perp} . Recalling that H_{\perp} at the upper part of the DW is opposite to the lower part of the circular DW arc as shown by Fig. 2(a), the initial difference Δv_{DW} of the DW speed between the upper and lower parts of the DW basically follows the relation $\Delta v_{\text{DW}} = v_{\text{DW}}(H_{\perp}) - v_{\text{DW}}(-H_{\perp})$. To visualize Δv_{DW} , $v_{\text{DW}}(-H_{\perp})$ is plotted by the gray dashed line in Fig. 5(b) together with $v_{\text{DW}}(H_{\perp})$ of the symbols with blue line. Then, Δv_{DW} corresponds to the vertical difference between these two lines (purple arrow). It is again seen from the figure that the sign of Δv_{DW} is reversed across a threshold magnetic field H_{\perp}^{th} (green vertical line). Thus, for the case that H_{\perp} is smaller than H_{\perp}^{th} , the DW rotates counterclockwise with $\Delta v_{\text{DW}} < 0$ and *vice versa*, in accordance to the observation from Fig. 5(d). Figure 5(e) shows the plot between θ_{tilt} and $\Delta(\ln v_{\text{DW}})$ for Sample IV. A clear correlation supports the validity of our model. Therefore, it is confirmed again that the direction of the DW tilting is truly determined directly by the asymmetry of the v_{DW} variation.

Discussion

There remain several challenging issues towards full analytic description of the DW tilting angle θ_{tilt} . First, we consider the effect of H_{\parallel} . Since the sign and magnitude of H_{\parallel} at both the upper and lower parts of the DW are the same as seen by Fig. 2(a), the difference should be mainly attributed to the opposite sign of H_{\perp} . For the case near the Bloch-type configuration, by applying the first-order Taylor expansion with respect to ψ , the DW energy density σ_{DW} becomes $\sigma_0 - \frac{1}{2}\pi\lambda M_S[(H_{\perp} + H_{\text{DMI}})^2 + 2H_S|H_{\parallel}|]/(H_S + |H_{\parallel}|)$ with the first leading terms of H_{\perp} and H_{\parallel} , where the DW anisotropy field H_S is defined as $4K_D/\pi M_S$. The difference $\Delta\sigma_{\text{DW}}$ is then given by $-\pi\lambda M_S H_{\perp}^+[H_{\text{DMI}}/(H_S + |H_{\parallel}|)]$, where H_{\perp}^+ denotes H_{\perp} at the upper parts of the DW. Note that $\Delta\sigma_{\text{DW}}$ is directly proportional to H_{\perp}^+ , but less sensitive to H_{\parallel} . Similarly, for the case near the Néel-type configuration with a large H_{DMI} , $\Delta\sigma_{\text{DW}} \cong -\frac{1}{2}\pi\lambda M_S H_{\parallel}[H_{\parallel}/(H_{\text{DMI}} + H_{\perp})]$, which is negligible due to the small ratio of $H_{\parallel}/(H_{\text{DMI}} + H_{\perp})$. Therefore, one can conclude that the direction of the DW tilting is mainly governed by the sign of H_{\perp} , whereas H_{\parallel} might adjust the tilting angle slightly.

Second, though the mechanism discussed with Δv_{DW} successfully explains the direction of the DW tilting as seen in Fig. 5(e), it is worthwhile to consider that there should be a restoring force to reach an equilibrium state with a finite θ_{tilt} . It is clear that the DW tension induces the restoring force, since the DW tension energy increases as the DW tilts. The role of the tension-induced force can be roughly estimated as follows. The DW tension energy E_{tension} is given by $E_{\text{tension}} = \sigma_{\text{DW}} w t \sec \theta_{\text{tilt}}$ as a function of θ_{tilt} within the assumption of

a straight DW, where w and t are the wire width and thickness, respectively. When the DW tilts from θ_{tilt} to $\theta_{\text{tilt}} + \delta\theta$, the upper and lower parts of the DW has the variation $\delta E_{\text{tension}}^{\pm}$ as given by $\frac{1}{2}\sigma_{\text{DW}}wt\delta\theta \sec\theta_{\text{tilt}} \tan\theta_{\text{tilt}}$, where the superscripts, $+$ and $-$, indicate the upper and lower parts of the DW, respectively. Similarly, the Zeeman energy has the variation $\delta E_{\text{Zeeman}}^{\pm}$ by $\pm\frac{1}{2}M_{\text{S}}H_{\text{z}}w^2t\delta\theta \sec^2\theta_{\text{tilt}}$. Comparing these two energy variations, one can get the relation of the tension-induced effective magnetic field H_{z}^{\pm} as $H_{\text{z}}^{\pm} = \pm\sigma_{\text{DW}} \sin\theta_{\text{tilt}}/M_{\text{S}}w$. For the case of a counterclockwise DW tilting (i.e. $\theta_{\text{tilt}} > 0$), a positive H_{z}^{+} enhances the DW speed of the upper part while a negative H_{z}^{-} reduces the DW speed of the lower part, resulting in clockwise rotation and *vice versa*. Therefore, the DW tension exerts a restoring force on the DW. The equilibrium θ_{tilt} is then determined by the steady-state condition i.e. $v_{\text{DW}}(H_{\perp}^{+}, H_{\text{z}} + H_{\text{z}}^{+}) = v_{\text{DW}}(H_{\perp}^{-}, H_{\text{z}} + H_{\text{z}}^{-})$. Though an analytic solution of the present condition is not available due to the yet unknown nature of the chirality-induced v_{DW} asymmetry, the empirical solution can be possibly provided by analyzing the two-dimensional map of $v_{\text{DW}}(H_{\perp}, H_{\text{z}})$ measured as a function of H_{\perp} and H_{z} .

In summary, we investigate here the DW tilting mechanism under application of in-plane magnetic field. For this study, four typical samples—Sample I (with DMI, but without chirality-induced asymmetry), Sample II (without both DMI and chirality-induced asymmetry), Sample III (without DMI, but with chirality-induced asymmetry), and Sample IV (with both DMI and chirality-induced asymmetry)—are examined. The experimental results clearly manifest that the DW tilting is triggered by the DW pinning at the structure edge and then, the direction of the DW tilting is governed by the DW speed asymmetry, whatever the origin of the asymmetry—either the DMI [9] or chirality-induced mechanisms [12-17]—is. The angle of the DW tilting is determined by the counterbalance between the DW speed asymmetry and the DW tension. A theory based on the DW speed asymmetry is provided.

Method

Sample preparation. The sample structures are 2.5-nm Pt/0.9-nm Co/2.5-nm Cu/1.5-nm Pt (Sample I), 4.0-nm Pt/0.3-nm Co/1.5-nm Pt (Sample II), 2.5-nm Pt/0.5-nm Co/1.5-nm Pt (Sample III), and 2.5-nm Pt/0.9-nm Co/2.5-nm Al/1.5-nm Pt (Sample IV), respectively. These samples are chosen as the representatives of typical major properties: Sample I (with DMI, but without chirality-induced asymmetry), Sample II (without both DMI and chirality-induced asymmetry), Sample III (without DMI, but with chirality-induced asymmetry), and Sample IV (with both DMI and chirality-induced asymmetry). These samples were deposited by use of dc magnetron sputtering on Si substrates with 100-nm-thick SiO₂ and 5-nm-thick Ta buffer layers. To enhance sharpness of the layer interfaces, each layer was deposited at a low deposition rate ($\sim 0.25 \text{ \AA/s}$) under an Ar sputtering pressure ($\sim 2 \text{ mTorr}$).

Observation of magnetic domain and DWs. The magnetic domains are observed by use of a magneto-optical Kerr effect microscope which has $500 \mu\text{m} \times 375 \mu\text{m}$ field of view. The observed images are captured by a low light level CCD camera. To apply in-plane and out-of-plane magnetic field, 2-axis electromagnets are attached to the system. The maximum magnetic field strengths for each axis are 38 and 200 mT along the z and x axes, respectively. The two electromagnets are carefully aligned to avoid any possible cross-talk between two magnetic fields. At first the magnetization of the magnetic wire is saturated to the single down domain. Next, the up domain is nucleated by application of the local Oersted's field generated by injecting currents (up to 0.5 A) in to the gold wire, which is perpendicular to the magnetic wire. Then external magnetic field is applied to propagate the generated up domain. The image of the propagating domain is captured with a constant time interval to determine the speed of the DW.

Acknowledgements

This work was supported by grants from National Research Foundations of Korea (NRF) funded by the Ministry of Science, ICT and Future Planning of Korea (MSIP) (2015R1A2A1A05001698 and 2015M3D1A1070465). Y.-K.P. and B.-C.M. were supported by the National Research Council of Science & Technology (NST) (Grant No. CAP-16-01-KIST) by the Korea government (MSIP). D.-H.K. was supported from Overseas researcher under Postdoctoral Fellowship of Japan Society for the Promotion of Science (Grant No. P16314).

References

- [1] S.-H. Yang, K.-S. Ryu, and S. Parkin, *Nat. Nanotech.* **10**, 221-226 (2015).
- [2] I. M. Miron, T. Moore, H. Szambolics, L. D. Buda-Prejbeanu, S. Auffret, B. Rodmacq, S. Pizzini, J. Vogel, M. Bonfim, A. Schuhl, and G. Gaudin, *Nat. Mater* **10**, 419-423 (2011).
- [3] A. Fert, V. Cros, and J. Sampaio, *Nat. Nanotech* **8**, 152-156 (2013).
- [4] T. Schulz, R. Ritz, A. Bauer, M. Halder, M. Wagner, C. Franz, C. Pfleiderer, K. Everschor, M. Garst, and A. Rosch, *Nat. Phys.* **8**, 301-304 (2012).
- [5] S. S. P. Parkin, M. Hayashi, and L. Thomas, *Science* **320**, 190 (2008).
- [6] D. A. Allwood, G. Xiong, C. C. Faulkner, D. Atkinson, D. Petit, and R. P. Cowburn, *Science* **309**, 1688-1692 (2005).
- [7] M. Hayashi, L. Thomas, R. Moriya, C. Rettner, and S. S. P. Parkin, *Science* **320**, 209-211 (2008).
- [8] A. Thiaville, S. Rohart, E. Jué, V. Cros, and A. Fert, *Europhys. Lett.* **100**, 57002 (2012).
- [9] S.-G. Je, D.-H. Kim, S.-C. Yoo, B.-C. Min, K.-J. Lee, and S.-B. Choe, *Phys. Rev. B* **88**, 214401 (2013).
- [10] O. Boulle, S. Rohart, L. D. Buda-Prejbeanu, E. Jué, I. M. Miron, S. Pizzini, J. Vogel, G. Gaudin, and A. Thiaville, *Phys. Rev. Lett.* **111**, 217203 (2013).
- [11] E. Jué, A. Thiaville, S. Pizzini, J. Miltat, J. Sampaio, L. D. Buda-Prejbeanu, S. Rohart, J. Vogel, M. Bonfim, O. Boulle, S. Auffret, I. M. Miron, and G. Gaudin, *Phys. Rev. B* **93**, 014403 (2016).

- [12] R. Lavrijsen, D. M. F. Hartmann, A. van den Brink, Y. Yin, B. Barcones, R. A. Duine, M. A. Verheijen, H. J. M. Swagten, and B. Koopmans, *Phys. Rev. B* **91**, 104414 (2015).
- [13] E. Jué, C. K. Safeer, M. Drouard, A. Lopez, P. Balint, L. Buda-Prejbeanu, O. Boulle, S. Auffret, A. Schuhl, A. Manchon, I. M. Miron, and G. Gaudin, *Nat. Mater.* **15**, 272 (2016).
- [14] C. A. Akosa, I. M. Miron, G. Gaudin, and A. Manchon, *Phys. Rev. B* **93**, 214419 (2016).
- [15] D.-Y. Kim, D.-H. Kim, and S.-B. Choe, *Appl. Phys. Express* **9**, 053001 (2016).
- [16] D.-H. Kim, S.-C. Yoo, D.-Y. Kim, B.-C. Min, and S.-B. Choe, *arXiv:1608.01762* (2016).
- [17] D. Lau, V. Sundar, J.-G. Zhu, and V. Sokalski, *Phys. Rev. B* **94**, 060401(R) (2016).
- [18] I. Dzyaloshinsky, *J. Phys. Chem. Solids* **4**, 241-255 (1958).
- [19] T. Moriya, *Phys. Rev.* **120**, 91 (1960).
- [20] S. Mühlbauer, B. Binz, F. Jonietz, C. Pfleiderer, A. Rosch, A. Neubauer, R. Georgii, and P. Böni, *Science* **323**, 915-919 (2009).
- [21] M. Heide, G. Bihlmayer, and S. Blügel, *Phys. Rev. B* **78**, 140403(R) (2008).
- [22] D.-Y. Kim, D.-H. Kim, J. Moon, and S.-B. Choe, *Appl. Phys. Lett.* **106**, 262403 (2015).
- [23] P. P. J. Haazen, E. Murè, J. H. Franken, R. Lavrijsen, H. J. M. Swagten, and B. Koopmans, *Nat. Mater.* **12**, 299 (2013).
- [24] K.-S. Ryu, L. Thomas, S.-H. Yang, and S. Parkin, *Nat. Nanotech.* **8**, 527 (2013).
- [25] D.-S. Han, N.-H. Kim, J.-S. Kim, Y. Yin, J.-W. Koo, J. Cho, S. Lee, M. Klaui, H. J. M. Swagten, B. Koopmans, and C.-Y. You, *Nano Lett.* **16** (7), 4438 (2016).
- [26] J. Cho, N.-H. Kim, S. Lee, J.-S. Kim, R. Lavrijsen, A. Solignac, Y. Yin, D.-S. Han, N. J. J. van Hoof, H. J. M. Swagten, B. Koopmans, and C.-Y. You, *Nat. Commun.* **6**, 7635 (2015).

- [27] F. C. Ummelen, N. H. J. Wilting, R. Lavrijsen, H. J. M. Swagten, and B. Koopmans, “Dzyaloshinskii-Moriya interaction probed by domain-wall tilting”, The 9th International Symposium on Metallic Multilayers (2016).
- [28] F. Cayssol, D. Ravelosona, C. Chappert, J. Ferré, and J. P. Jamet, Phys. Rev. Lett. **92**, 107202 (2004).
- [29] A. Thiaville, Y. Nakatani, J. Miltat, and Y. Suzuki, Europhys. Lett. **69** (6), 990-996 (2005).
- [30] S. Lemerle, J. Ferré, C. Chaoert, V. Mathet, T. Giamarchi, and P. Le Doussal, Phys. Rev. Lett. **80**, 849 (1998).
- [31] G. Blatter, M. V. Feigel'man, V. B. Geshkenbein, A. I. Larkin, and V. M. Vinokur, Rev. Mod. Phys. **66**, 1125 (1994).
- [32] A. I. Larkin and Y. N. Ovchinnikov, J. Low Temp. Phys. **34**, 409 (1979).
- [33] S.-G. Je, S.-C. Yoo, J.-S. Kim, J. Moon, B.-C. Min, and S.-B. Choe, arXiv:1512.03405 (2015).

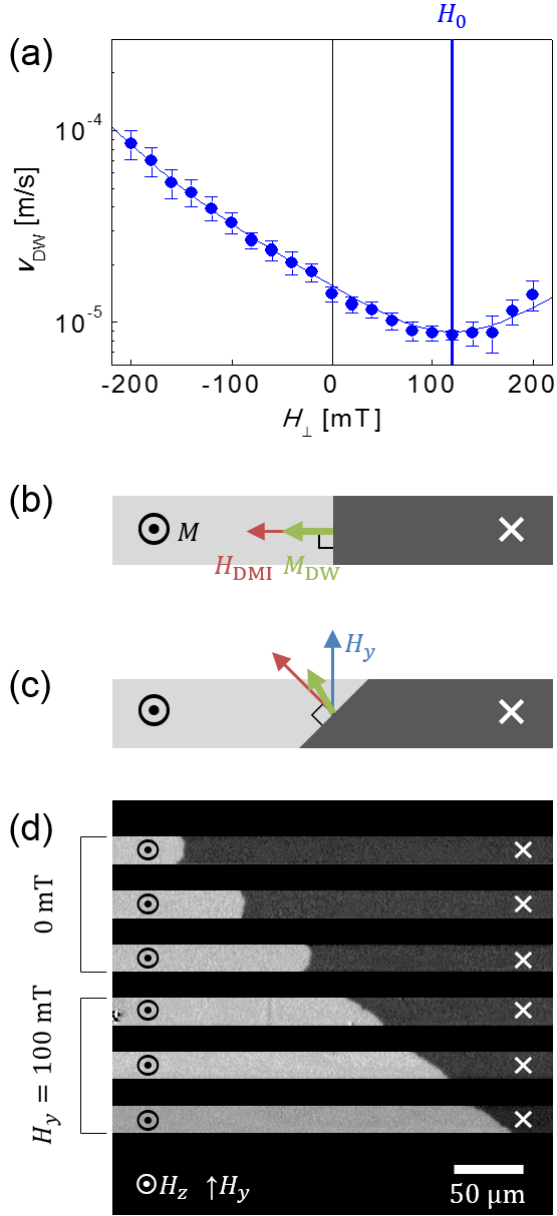


Figure 1 (a) Plot of v_{DW} as a function of H_{\perp} for the Sample I. Blue vertical line indicates the compensate field H_0 for the DMI-induced effective field H_{DMI} . Schematic diagram of the DW for the magnetic wire with negatively large H_{DMI} without (b) and with (c, 100 mT) application of H_y . Red, green, and blue arrows represent H_{DMI} , the magnetization inside the DW M , and applied H_y , respectively. (d) Image of the domains and DW for the micro-wire-patterned Sample I. First three and last three images show the propagating domain with and without application of H_y , respectively.

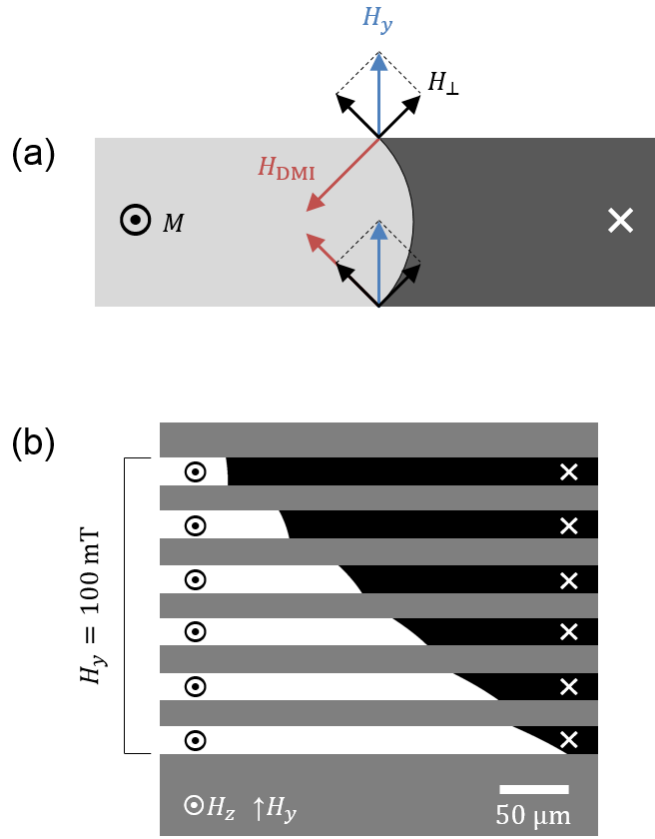


Figure 2 (a) Schematic diagram of the arc-like-shaped DW due to the strong wire-edge pinning. Each red and blue arrows represent H_{DMI} and H_y . Black arrows indicate perpendicular and parallel component of H_y (H_{\perp} and H_{\parallel}). (b) Results of the numerical simulation.

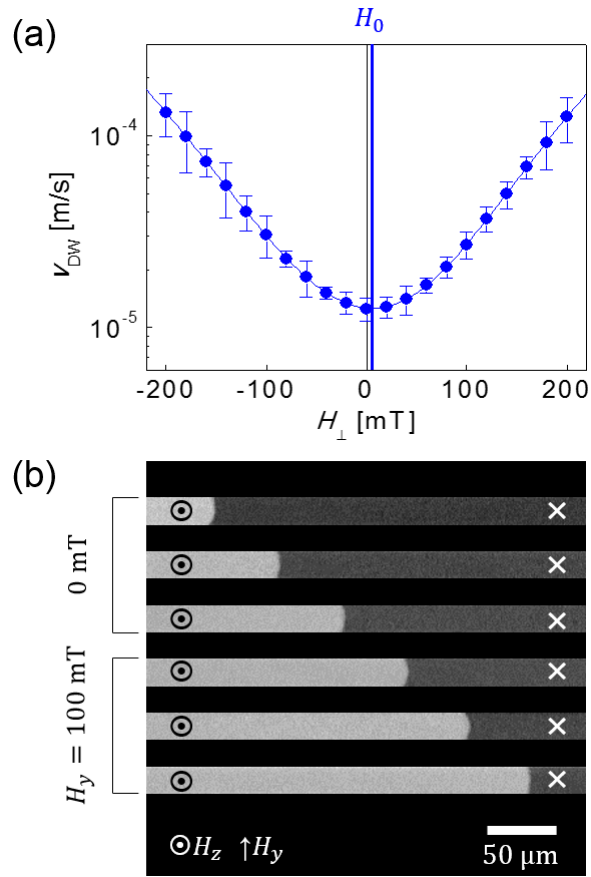


Figure 3 (a) Plot of v_{DW} as a function of H_{\perp} for the Sample II. Blue vertical line indicates H_0 . (b) Image of the domains and DW for the micro-wire-patterned Sample II. First three and last three images show the propagating domain without and with (100 mT) application of H_y , respectively.

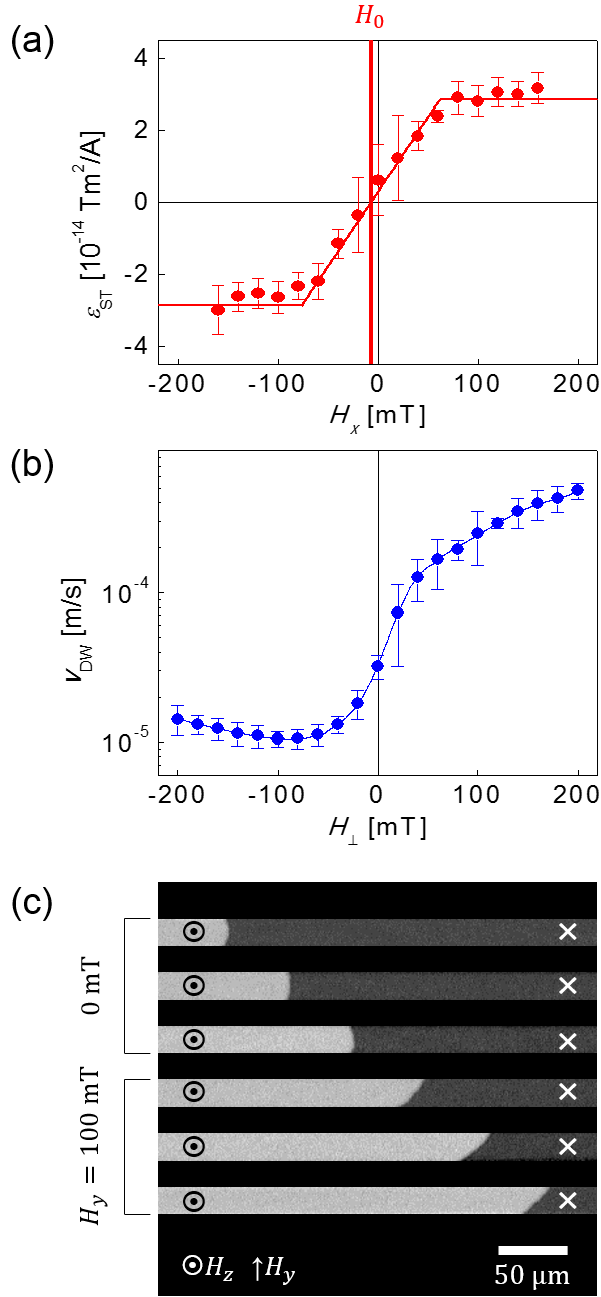


Figure 4 (a) Plot of spin-torque efficiency ε_{ST} as a function of H_x for the Sample III. Red vertical line indicates H_0 . (b) (a) Plot of v_{DW} as a function of H_{\perp} for the Sample III. (c) Image of the domains and DW for the micro-wire-patterned Sample III. First three and last three images show the propagating domain without and with (100 mT) application of H_y , respectively.

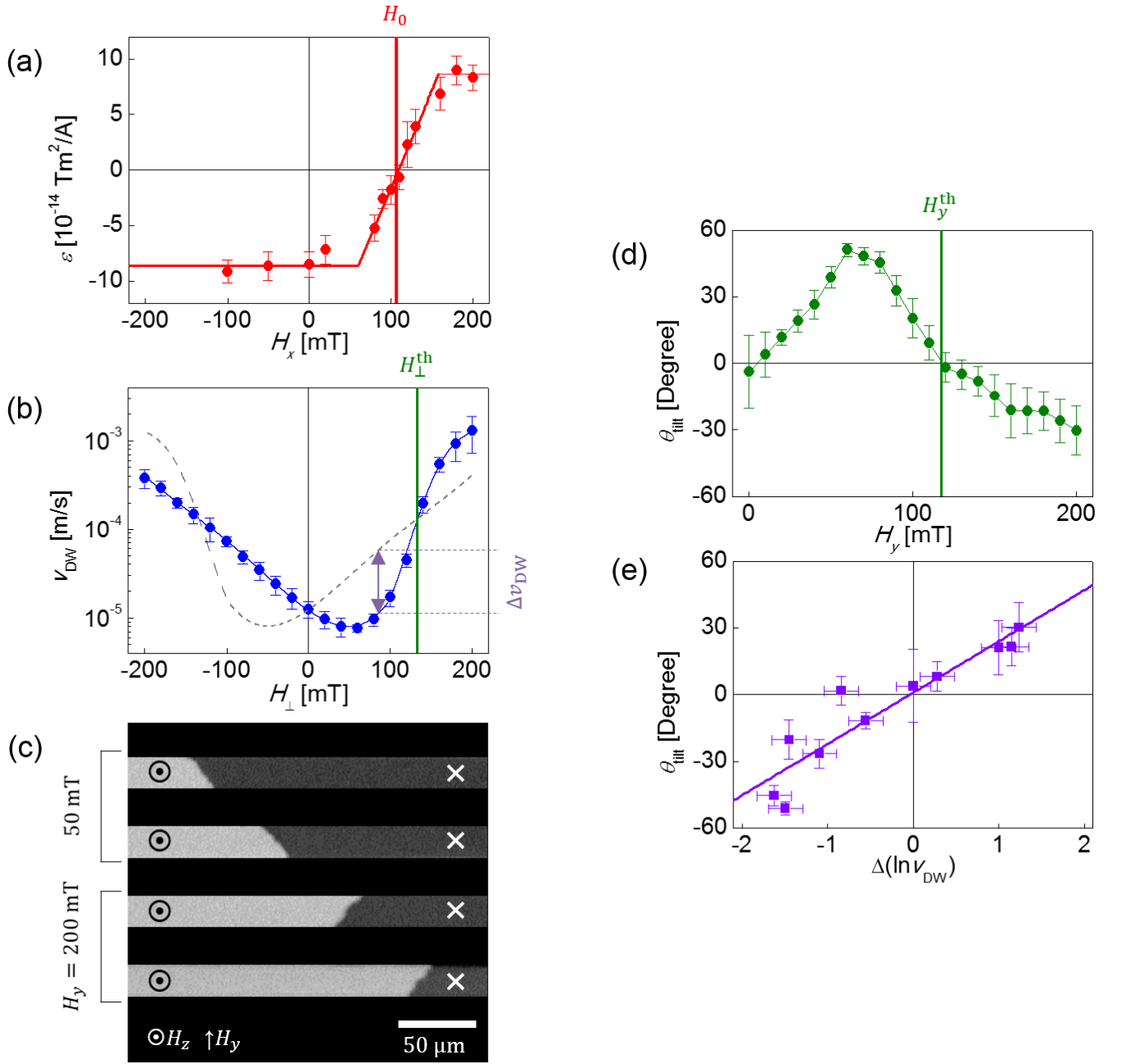


Figure 5 (a) Plot of spin-torque efficiency ε_{ST} as a function of H_x for the Sample IV. Red vertical line indicates H_0 . (b) (a) Plot of v_{DW} as a function of H_{\perp} for the Sample IV. Gray dashed line represents v_{DW} of the lower edge as a function of H_{\perp} . Green vertical line indicates H_{\perp}^{th} , where blue and dashed-gray curves intersect. (c) Image of the domains and DW for the micro-wire-patterned Sample IV. First two and last two images show the propagating domain under the application of $H_y = 50$ mT and $H_y = 200$ mT, respectively. (d) Plot of θ_{tilt} as a function of H_y . Green vertical line indicates H_y^{th} , where $\theta_{\text{tilt}} = 0$. (e) Plot of θ_{tilt} with respect to $\Delta(\ln v_{\text{DW}})$. The best linear fitting ($R^2 = 0.87$)

is presented by the purple solid line.